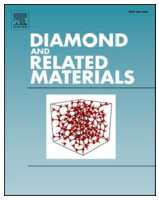
Diamond & Related Materials 167 (2026) 113823



Contents lists available at ScienceDirect

Diamond & Related Materials

journal homepage: www.elsevier.com/locate/diamond





Thermoelectric analysis of Pyrograf® III carbon nanofiber/polypropylene composites with considerable high positive Seebeck coefficients

A.J. Paleo [a,*], B. Krause [b], J.M. Mánuel [c], A.M. Beltrán [d], A.I. Ribeiro [a], Maria F. Cerqueira [e,f], E. Muñoz [g], M. Melle-Franco [h], S. Sanchez-Valdes [i], P. Pötschke [b]

[a] 2C2T-Centre for Textile Science and Technology, University of Minho, Campus de Azurém, 4800-058, Guimarães, Portugal
[b] Leibniz-Institut für Polymerforschung Dresden e.V. (IPF), Hohe Str. 6, 01069, Dresden, Germany
[c] Department of Condensed Matter Physics and Institute of Research on Electron Microscopy and Materials (IMEYMAT), Faculty of Sciences, University of Cádiz, Puerto Real, 11510, Cádiz, Spain
[d] Department of Materials and Transportation Engineering and Science, Escuela Politécnica Superior, Universidad de Sevilla, 41011, Sevilla, Spain
[e] INL—International Iberian Nanotechnology Laboratory, Av. Mestre, Jose Veiga, 4715-330, Braga, Portugal
[f] CFUM—Center of Physics of the University of Minho, Campus de Gualtar, 4710-057, Braga, Portugal
[g] Facultad de Física, Pontificia Universidad Católica de Chile, Santiago, 7820436, Chile
[h] CICECO – Aveiro Institute of Materials, Department of Chemistry, University of Aveiro, 3810-193, Aveiro, Portugal
[i] Centro de Investigación en Química Aplicada, Blvd Enrique Reyna 140, Saltillo, Coahuila, 25294, Mexico

ARTICLE INFO

Keywords:
Carbon nanofibers
Polypropylene
Electrical properties
Seebeck coefficient
Variable range hopping

ABSTRACT

This study presents, for the first time, the thermoelectric (TE) properties of as provided Pyrograf® III PR 24 HHT XT carbon nanofibers (CNFs) and their effect on the TE properties of polypropylene (PP) processed by melt mixing with 6% by weight of these CNFs. At 30 °C, the CNFs present a modest σ of ~37 S m^{-1} and a considerable high S of ~40 μVK^{-1}, equivalent to a power factor (PF) of 6 × 10^{-2} μW m^{-1} K^{-2}, which makes them the CNFs with the greatest TE properties among the others Pyrograf® III grades. As for the PP/CNF composites, they show lower σ and S at 30 °C, with values of ~7 × 10^{-2} S m^{-1}, and ~ 38 μVK^{-1}, respectively, equivalent to a PF of 1 × 10^{-4} μW m^{-1} K^{-2}. From the TE results of the CNFs and their derived PP/CNF composite, a simplified quantum chemical model is applied to investigate the transfer of electrons (n-type doping) from PP to CNFs, concluding that this transfer depends on the adsorption mode of PP molecules and CNFs at their interface. Moreover, the σ of the CNFs and PP/CNF composite show negative temperature effect (NTC) in the interval from 30 to 100 °C, explained as thermally activated hopping mechanism by the 3D variable range hopping (VRH) model, while their S shows nonlinear character, also observed in others Pyrograf® III grades and derived PP/CNF composites, in that interval of temperature. These results are presented with the aim of determining the role played by this type of CNFs, on the thermoelectric properties of the polymer composites melt mixed using them, with a view to their use as p-type materials in thermoelectric generators (TEGs).

1. Introduction

As non-renewable energy sources dependent on fossil fuels are depleted, the interest in producing energy from more sustainable sources has become mandatory, and it is in this sense that technologies based on thermoelectric (TE) devices, which transform a difference of temperature into a voltage difference, have become a promising alternative. In terms of efficiency, their evaluation is calculated through the figure of merit, $zT = \frac{S^2\sigma}{k} T$, where σ and k denote the electrical and the thermal conductivity, respectively, T defines the temperature in which the test is conducted, while the Seebeck effect (S) defines the ratio of the induced voltage to the applied T gradient between the cold and hot parts of the TE material [1]. It should be noted that the power factor (PF) defined as S^2 σ, is often used for obtaining the TE effectiveness. Furthermore, TE materials have negative or positive S, depending on whether the electrical potential originated comes from negative (electrons) or positive (holes) charge carriers [2]. In this regard, it is well known that inorganic materials such as those based on BiTe series have been extensively investigated because of their high zT [3]. However, despite their superior zT, they suffer from some drawbacks arising from their toxicity and

* Corresponding author.
E-mail address: ajpaleovieito@2c2t.uminho.pt (A.J. Paleo).

https://doi.org/10.1016/j.diamond.2026.113823
Received 4 March 2026; Received in revised form 20 May 2026; Accepted 2 June 2026
Available online 9 June 2026
0925-9635/© 2026 The Authors. Published by Elsevier B.V. This is an open access article under the CC BY license (http://creativecommons.org/licenses/by/4.0/).

the fact that they are scarce elements, which severely limits their practical applications [4,5]. For this reason, organic TE materials based on intrinsically conductive polymers, as well as insulating polymers filled with conductive metal or carbon particles, such as carbon nanotubes (CNTs), have become an alternative approach [6,7]. The latter, known as conductive polymer composites (CPCs), are attracting interest as n-type or p-type materials required to build the thermoelectric modules of TE generators (TEGs), due to the good balance of properties they offer, combining the low k and the flexibility of the polymer with the high S and σ of the carbon particles required to achieve high levels of zT [8,9]. More in particular, polypropylene (PP), among other insulating polymers, is widely used in the manufacture of CPCs because its ease of large-scale processing and low economic cost [10]. As for the conductive carbon particles used in CPCs, the aforementioned CNTs are a very attractive option due to their high aspect ratio consisted of large length and small diameters [11,12], which allows them to achieve high σ at low percolation thresholds when dispersed homogeneously in the polymer [13]. In general terms, the σ in CPCs follows the equation $\sigma \propto (\phi - \phi_c)^t$, for $\phi > \phi_c$, with ϕ as the volume fraction of the carbon particle, and t is a critical exponent [14]. This means that it is possible to precisely adjust the σ in CPCs, since below ϕ_c, the σ of CPCs should have the σ of the polymer, while above ϕ_c, the σ of CPCs should have the σ of the carbon particles. Conversely, less is known on the Seebeck coefficient of CPCs. For instance, contrary to expectations, PP melt mixed with 2% by weight of commercial CNTs showed larger values of S than the CNTs themselves with which they were produced [15]. More recently, the influence of two Pyrograf® III carbon nanofibers (CNFs) on the S of their melt mixed PP/CNF compounds revealed an electron donation from the CNFs to the PP molecules, suggesting that similar electron donation could be found from CNTs to the PP in PP/CNT composites [16]. Regarding this type of CNFs, it should be noted that the grades of Pyrograf® III available on the market vary according to diameter (PR 19 ~ PR 25 > PR 24), and the thermal treatment to which they have been subjected after their growth by chemical vapor deposition (CVD) from the lowest to the highest temperatures, respectively (PS, LHT or HHT) [17]. While previous studies have investigated the effect of Pyrograf® III PR 24 LHT XT and PR 19 LHT XT on the σ and S of their melt mixed PP/CNF composites [18], this study expands those results, and it presents for the first time the effect of Pyrograf® III PR 24 HHT XT, a type of nanofiber that is much more graphitic and has fewer impurities than Pyrograf® III PR 24 LHT XT and PR 19 LHT XT studied previously, on the σ and S properties of its derived PP/CNF melt mixed composite. In particular, the investigation of the σ and S from room temperature up to ~100 °C of the as provided CNFs and of their derivative melt mixed PP with 6 wt% of CNFs are introduced herein, while the experimental results have been complemented with theoretical frameworks such as electronic charge transfer modeling, the variable range hopping [19] and nonlinear Seebeck models [20], with the goal of comprehending better the physical origin of them. This study helps to understand the effect that these types of CNFs have on the Seebeck coefficient of the CPCs produced using them.

2. Materials and methods

2.1. Materials and processing

Isotactic PP (Valtec PP-HP423), MFI 3.8 g/10 min was obtained from Indelpro Company. The Pyrograf® III PR 24 HHT XT were received from Applied Sciences Inc. (Cedarville, OH, USA). They are synthesized by CVD and then subjected to temperatures of 3000 °C in order to achieve high graphitization and to remove as much of the catalytic iron used for their synthesis as possible (reaching <100 ppm). As is the case with all these CNFs, they show hollow cores and total diameters of 100 to 150 nm, 50 to 200 μm in length and a surface area of 41 $m^2\ g^{-1}$ [21]. Both the CNFs and the PP have been used as they arrived [17].

PP composites with 6 wt% of CNFs (above ϕ_c) were processed by shear mixing in a Brabender Plasti Corder System at a temperature of 190 °C for 15 min, using 75 rpm as rotational speed [22]. Then, the PP/CNF composite was formed by compression molding. For that, the granulated composite batch was compression-molded at 15 ton and at temperatures of 180 °C. At the end, films of (15 × 15) cm^2 and thicknesses of ~3 mm were used for analysis. For the remainder of the study, the PP with 6 wt% of CNFs will be labeled to as the PP/CNF composite.

2.2. Characterization methods

Detailed information on the morphology and crystalline structure of CNFs was analysed with Transmission Electron Microscopy (TEM), conventional TEM (CTEM) and atomically resolved TEM (HRTEM). To this purpose, a TALOS S200 STEM microscope (ThermoFischer Scientific, Waltham, MA, USA), available at the University of Seville Research, Technology and Innovation Centre (CITIUS, Universidad de Sevilla, Spain) was utilized. The electron beam was accelerated at 200 kV, and a 40-μm-diameter objective aperture was utilized in order to obtain HRTEM images. The same instrument, working in Scanning-TEM mode (STEM), also allowed a compositional characterization of the nanofibers, via chemically sensitive images (High Angle Annular Dark Field micrographs, or HAADF) and Energy Dispersive X-ray Spectroscopy (EDX) maps.

The surface of strands of the PP/CNF samples were layered with 3 nm platinum and cryo-fractured in liquid nitrogen before taking the images at 3 kV through scanning electron microscope (SEM) (Ultra plus microscope, Carl Zeiss GmbH, Germany, field emission cathode).

The thermal response and crystallization characteristics of PP and PP/CNF was studied by Differential Scanning Calorimetry (DSC) on a DSC Discovery instrument at 10 °C min^{-1} in nitrogen atmosphere of 50 ml min^{-1}. First, an initial thermal heating of 0–200 °C was performed to delete the thermal history, followed by a thermal cooling of 200–0 °C to obtain the enthalpy and temperature of crystallization, and at the end, a second heating of 0–200 °C was carried out to record the enthalpy and temperature of fusion. Thermogravimetric analysis (TGA) was conducted on a TA Instrument TGAQ500 at 10 °C min^{-1} under nitrogen atmosphere.

The TE measurements were carried out at IPF Dresden using a self-constructed device combined with Keithley multimeter DMM2001 [23], and the schema of the device as well as the procedure of measurement is reported in Krause et al. [24]. The volume conductivity and thermovoltage were programed at temperatures from 30 to 96 °C. Temperature differences of −8 K, −4 K, +4 K and + 8 K were set for each temperature step, and the Seebeck coefficient was calculated from these four thermoelectric voltages. The measurements were repeated up to five times. The electrical resistance was measured when there was no temperature gradient across the sample. The measurements were carried out on two sample pieces, and the average Seebeck coefficient, volume conductivity and power factor were calculated from these. The end points of the samples were coated with silver paste for getting better metallic contact with the device. The thermal conductivity k of the PP/CNF composite was calculated from specific heat capacity, the density (determined by buoyancy method) and the thermal diffusivity. The thermal diffusivity was measured on compression molded rectangle samples (10 mm × 10 mm, thickness 1 mm) through the plate thickness using the light flash apparatus LFA 447 NanoFlash (Netzsch-Gerätebau GmbH, Selb, Germany) at the same temperatures used for measuring the volume conductivity and thermovoltage. The specific heat capacity was measured by comparing the heights of each specimen with Pyroceram 9606 [25].

Hall effect analysis was used for obtaining the majority carriers, the carrier concentration (p) and mobility (μ) of PP/CNF composite. For that, a Keithley 2410 Source Meter and 2182 Voltmeter, together with a GMW 5403FG electromagnet (magnetic field up to 1 T) was used. All tests were done at room temperature using +500 mT and − 500 mT on 2

cm × 2 cm samples. A LabVIEW program was used for data acquisition, before analysis, the proper functioning of electrical contacts was verified by the Van der Pauw method.

2.3. Electronic charge transfer modeling

In this work, a simplified quantum chemical model was applied to discuss the impact of PP on the CNF graphitic layers, following a previous study in which the charge transfer and molecular geometry of finite PP polymers filtered on finite hexagonal graphene monolayers was calculated [16]. More precisely, an isotactic PP oligomer with 20 monomeric units adsorbed onto a graphene bilayer of 5.6 nm diameter and 912 atoms per layer adsorbed on two basal locations, far and near the graphene flake edge, and adsorbed perpendicular to a flake edge was computed (Fig. 1). For computational efficiency, molecular optimizations were performed with the GFN-FF Hamiltonian [26], while the charges were computed with the GFN1-xTB Hamiltonian which allowing to address thousands of atoms [27]. The charge transfer was computed by adding up the CM5 partial charges [28] of PP and the two hexagonal graphene flakes. Relevantly, the combined methodology xTB-GFN1/GFN-FF, while showing enhanced computational efficiency was benchmarked to yield very similar charge transfer to our previous model of PP on monolayer hexagonal graphene flakes at the GFN1-xTB level [16]. All calculations were performed with the xTB software v6.7.0. [29].

3. Results and discussion

3.1. Morphological and compositional characterization

Fig. 2a shows a CTEM image, obtained in Bright Field conditions, of a section of a CNF, in which the tubular morphology of the material is evident. The intensity contrast in this type of TEM micrographs indicates a difference in the orientation of crystalline plane, which is expected since the graphite bends to form the tube. The atomic planes of the CNF are visible in greater detail at Fig. 2b, showing a HRTEM image from one of the regions in Fig. 2a. All the planes in this image present atomic distances between 3.3 and 3.4 Å, which agrees well with the theoretical distances associated to the atomic plane (002) of the hexagonal graphite [30,31]. Fig. 2b includes an inset of a zoomed area from these atomic planes, as an example of the measured atomic distances. Regarding the chemical composition, EDX maps were obtained from single CNFs. Fig. 2 also shows a HAADF micrograph, where the intensity contrast can be associated to the cylindrical, hollow shape of the CNF, since the intensity in these STEM images indicates a change in the amount of material in the electron beam path, as well as a change in composition. EDX maps indicate that these nanofibers are composed by C atoms, since other signals for elements (for example, Si or O) yield only noise.

Fig. 3 shows micrographs with different magnifications of the PP/CNF sample. At the lowest magnification (Fig. 3a), a large area of the sample can be observed in which no agglomerates are visible, suggesting that adequate dispersion has been achieved. As the resolution is increased (Fig. 3b and c), some holes can be seen where the CNFs were attached before fracture and which detached when the sample fractured, which can infer to poor adhesion between the polymer and the particles. However, there are also other cases in which the CNFs remain adhered to the matrix, so the existence of intermolecular interactions between them cannot be ruled out.

3.2. Thermal characterization

DSC and TGA measurements were used in order to examine the thermal stability of PP with and without CNFs. Regarding the DSC thermograms of the samples, narrower curves in the PP/CNF than in the control PP were observed (Fig. 4a). This can be attributed to a distribution of lamellar thicknesses in the polymer due to the presence of CNF, which homogenizes the size of the crystals and results in a decrease in spherulitic morphology size [32]. In addition, a slightly higher melting peak temperature (T_m) in the PP/CNF sample than PP, from 163.6 to 165 °C, was noticed (Fig. 4a and Table 1). Moreover, an increase of 19 °C in crystallization temperature (T_c) of PP/CNF is observed compared to the T_c of the PP (Fig. 4b and Table 1). This can be attributed to the presence of CNF due to their role as nucleating agents in the crystallization of PP [33]. However, the degree of crystallinity (ΔX_c) of the PP/CNF composite:

$$\Delta X_c = \frac{\Delta H_m}{\Delta H_0 f_{PP}(1 - \%CNF)} \times 100\% \quad (1)$$

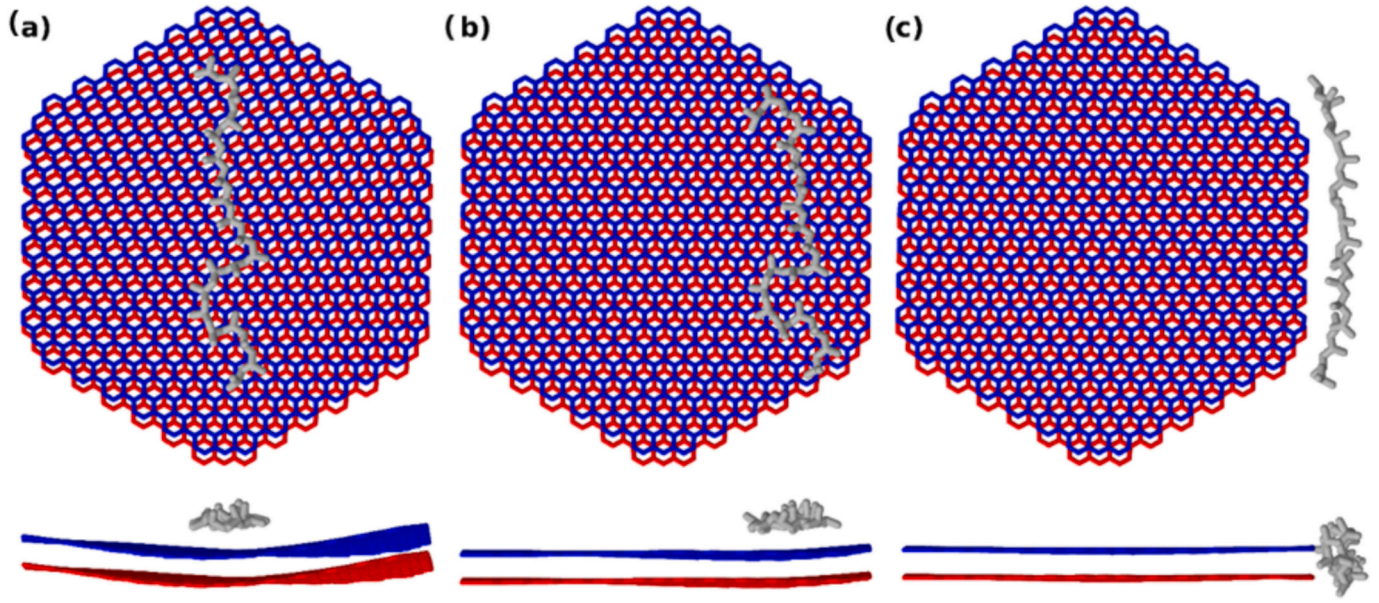


Fig. 1. Molecular models of the central basal adsorption (a) near-edge basal adsorption; (b) and edge adsorption; (c) of isotactic 20-mer polypropylene, rendered as grey sticks, adsorbed onto two AB-stacked $C_{834}H_{78}$ hexagonal graphene flakes, rendered as blue and red sticks, computed with the GFN-FF Hamiltonian. Hydrogen atoms have been omitted for clarity. (For interpretation of the references to colour in this figure legend, the reader is referred to the web version of this article.)

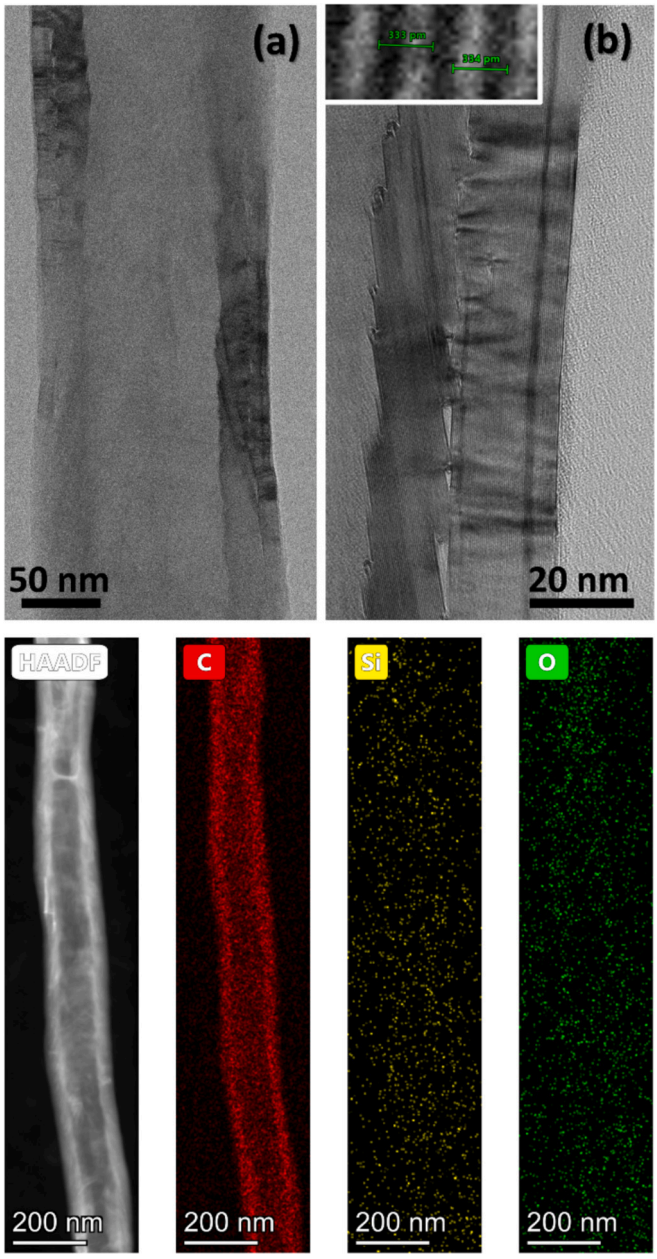


Fig. 2. Micrographs for a representative single CNF: (a) CTEM-Bright Field mode; and (b) HRTEM. Below, HAADF image and EDX maps for C, Si and O signals.

where ΔH_m and $\Delta H_0 f_{PP}$, are the melting enthalpy of the PP, and the 100% crystalline PP (209 J g^{-1}) [34], respectively, decreased when compared with neat PP, from 45 to 42.5%. In this case, the CNF may restrict the mobility of the PP, creating obstacles to the movement of polymer chains, and preventing them from fully organizing into crystalline regions [35].

The TGA data clearly demonstrate the improved stability of the PP/CNF composite, where neat PP loses 30% of its weight at 368 °C, while for the PP/CNF composite, this occurs only at 436 °C (Fig. 5a, Table 2). It is also possible to deduce that the amount of CNF present in the PP/CNF is higher than the expected 6 wt%, possibly due to local differences in CNF distribution within the sample, which may result in a higher CNF concentration in the analysed region. As indicated in the DTG (Fig. 5b), the initial degradation of the PP/CNF composite showed a rise of 75 °C with respect to the PP, while its maximum degradation temperature was also increased by 41 °C (Fig. 5b). Lastly, at 10, 30 and 50% weight loss, the decomposition temperature ranged from 337 to 388 °C for neat PP, and from 420 to 445 °C for the PP/CNF, indicating a significant enhancement in thermal stability of approximately 20% (Table 2).

3.3. *Thermoelectric properties at 30 °C*

Table 3 shows the σ at 30 °C of the samples. The σ (~ 37 S m^{-1}) of this carbon nanofiber (PR 24 HHT XT) is quite lower than the σ measured for PR 19 LHT XT and PR 25 PS XT (~ 136 S m^{-1}) [36,37] and PR 24 LHT XT (~ 133 S m^{-1}) [38] (Table S1 in Supplementary data). This lower σ is an unexpected result, as this Pyrograf® III grade (HHT) is heat treated at higher temperatures than LHT grade, which should guarantee higher σ values due to their higher degree of graphitization [17]. Consequently, it is not surprising that, given the fact that the σ found for this carbon nanofiber PR 24 HHT XT is lower than the σ measured for PR 19 LHT XT and PR 24 LHT XT, the σ of the PP/CNF composite (7×10^{-2} S m^{-1}) results lower than the σ of 15 and 50 S m^{-1} reported for polypropylene melt-mixed with 5 wt% of those PR 19 LHT XT [36] and PR 24 LHT XT [16], respectively (Table S1). Interestingly, similar values of σ (1×10^{-2} S m^{-1}) were measured for PP melt-mixed with 10 wt% of PR 24 PS XT [39], and it should be noticed that 10^{-4} S m^{-1} were achieved for epoxy composites mixed with 1.5 wt% of PR 24 HHT XT [40].

Table 3 shows the S at 30 °C of the samples. Notably, the PR 24 HHT XT analysed here, unlike other Pyrograf® III grades, which are n-type [36], shows positive Seebeck as most of CNTs [41]. However, in terms of absolute values, and, to the authors' knowledge, the S of these CNFs (40.6 μVK^{-1}) is the highest found for Pyrograf® III (Table S1), which makes them even comparable to the Seebeck of SWCNTs Tuball™ [15]. It is noticed that the PP/CNF composite keeps the p-type of the CNFs, though with a slightly lower S of 37.6 μVK^{-1} (Table 3). Accordingly, its S is the highest found for PP composites made with this type of CNFs (Table S1). Comparatively, the S of the composite analysed is lower than the 47.2 μVK^{-1} measured for PP with 2 wt% of SWCNTs Tuball™ [15].

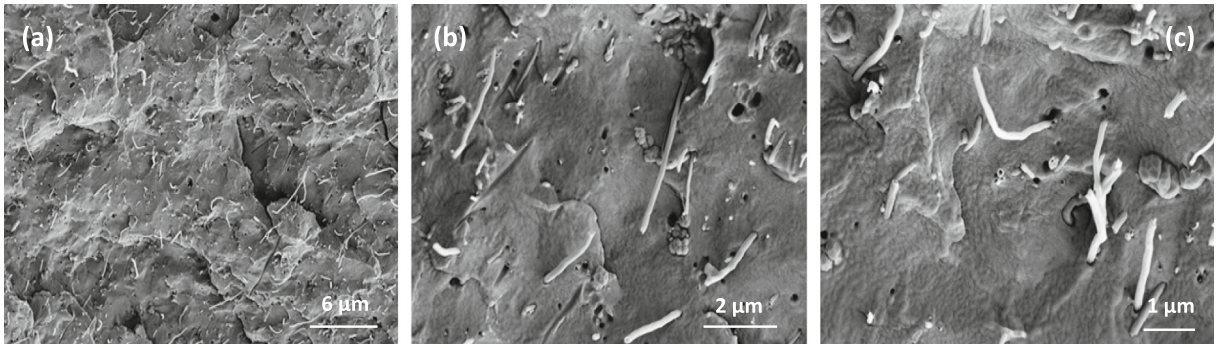


Fig. 3. SEM micrographs of the surface morphology of PP/CNF at different magnification scales.

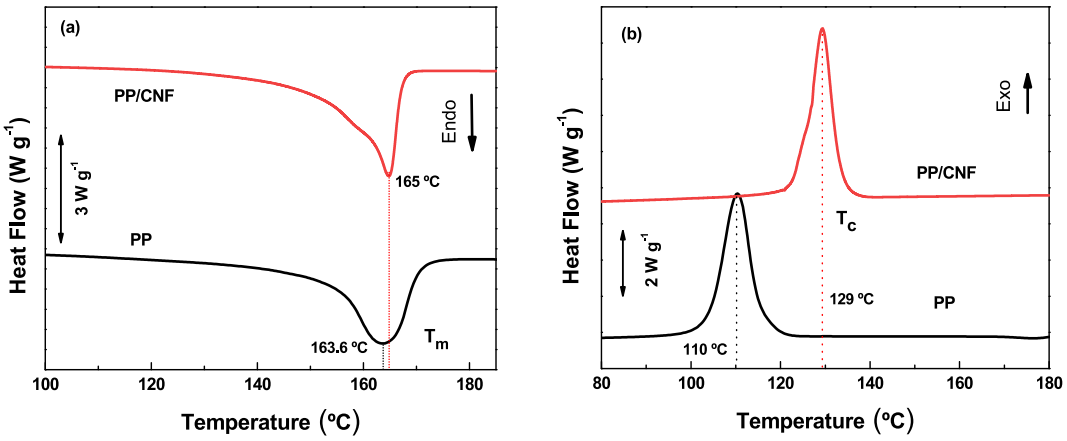


Fig. 4. DSC results: (a) 2th heating; (b) 1th cooling.

Table 1
DSC parameters.

Sample	T_m (°C)	T_c (°C)	ΔH_m (J g^{-1})	ΔX_c (%)
PP	163.6	110.0	99.0	45.0
PP/CNF	165.0	129.0	99.5	42.5

As discussed in previous studies [18], this change in the S of the composite with respect to the S of CNFs, leads to the PP being able to play its effect on the S value of the CNFs. However, in contrast to those previous works, which predict by the model presented in Section 2.3, that PP may withdraw electrons (p-type doping) to CNFs and CNTs [16], this result infers just the opposite: PP is donating electrons (n-type doping) to CNFs. This latter would imply a decrease in the p-type of the CNFs, and therefore cause the reduction in the value of Seebeck coefficient observed for the PP/CNF composite. Interestingly, the same effect (electron transfer from PP to MWCNTs) could explain the values of $-17.3\ \mu VK^{-1}$ found in certain composites of PP with 2 wt% of nitrogen-doped MWCNTs [15]. To investigate the charge transfer of polypropylene on the carbon nanofibers, as discussed in the Section 2.3, a single conformation for syndiotactic PP was used, as a previous study revealed a negligible tacticity and conformation dependence [16]. For both basal adsorptions computed (Fig. 1), a slight but quantifiable charge transfer from graphene to the PP molecules (0.002 electrons per monomer) was found, matching accurately the observations of previous report [16]. In contrast, the adsorption on a graphene edge yielded charge transfer in the opposite direction, from the PP molecule to graphene, of a comparable magnitude, 0.002 electrons per monomer. Although from highly idealized models, this indicates that the contact doping of PP with CNFs depends on the adsorption mode and contact interactions of PP molecules and CNFs at their interface. Therefore, unlike other Pyrograf® III grades with a lower degree of crystallinity such as PR 19 LHT XT and PR 24 LHT XT [18], it can be inferred that the PR 24 HHT XT produced with the highest levels of graphitization according to the manufacturer could promote electron transfer from the PP molecule to CNFs (n-type doping).

Table 3 introduces the carrier concentration *p* and mobility μ at room temperature of the composite, obtained as described in the Section 2.2, which also confirmed its p-type character, with values of $\sim 5 \times 10^{15}$ cm^{-3} and 60 $cm^2\ v^{-1}\ s^{-1}$ for its *p* and μ, respectively, which do not differ from the values found for PP composites produced with Pyrograf® III PR 24 LHT XT [16].

Table 2
Temperature for different percentages of weight loss of PP and PP/CNF composite.

Sample	$T_{(-10\%)}$ (°C)	$T_{(-30\%)}$ (°C)	$T_{(-50\%)}$ (°C)
PP	337	368	388
PP/CNF	420	436	445

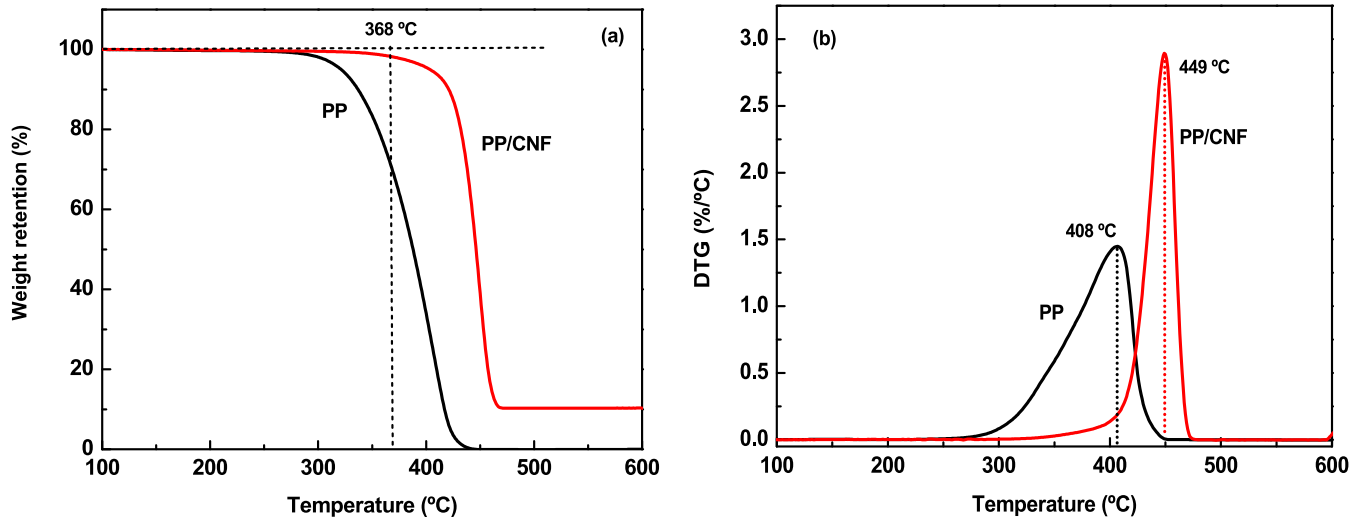


Fig. 5. Thermal characterization: (a) TGA; and (b) DTG curves.

Table 3
σ, S, p PF, zT, *p*, and μ of PP/CNF composite at 30 °C (results of CNFs were measured at 31 °C).

Sample	σ (S m^{-1})	S (μV K^{-1})	PF (μW m^{-1} K^{-2})	zT	*p* (cm^{-3})	μ (cm^2 v^{-1} s^{-1})
PP/6 wt% CNF	0.07 ± 0.06	37.6 ± 0.4	1.0×10^{-4}	6.1×10^{-8}	$5.4 \pm 0.4 \times 10^{15}$	60 ± 20
CNF powder	37 ± 2	40.6 ± 0.2	6.1×10^{-2}	4.3×10^{-5}	–	–

Table 3 shows the PF and zT at 30 °C of the samples. The PF of the CNFs is 6.1×10^{-2} μW m^{-1} K^{-2}, and therefore is the highest PF measured for this type of Pyrograf® III CNFs (Table S1). However, the composite shows a PF of 1.0×10^{-4} μWm^{-1} K^{-2}, which is in the same order than the PF of 7×10^{-4} and 2×10^{-4} μWm^{-1} K^{-2} of PP with 5 wt% of PR 24 LHT XT and PR 19 LHT XT, respectively (Table S1). Notably, samples of PP with 2 wt% of NC 7000™ MWCNTs share the same PF of 1.0×10^{-4} μWm^{-1} K^{-2} [15]. For comparative terms, it is noted that PF of 0.78 μWm^{-1} K^{-2} has been already achieved in composites of PP with 7.5 wt% of boron-doped SWCNTs [42]. The zT at 30 °C of the CNFs is estimated by means of the k of 0.43 W m^{-1} K^{-1} reported on mats of Pyrograf® III [43], while zT at 30 °C of the composite was estimated from the k of 0.49 W m^{-1} K^{-1} measured as presented in 2.2. For the CNFs, a zT of 4.3×10^{-5} is estimated, which is the highest zT found for this type of CNFs (Table S1), and one order higher than the zT reported for certain MWCNT buckypapers [44]. It should be reminded that values of zT in the order of 10^{-1} have been already achieved for SWCNTs [11]. As mentioned at the start of this section, it is not surprisingly that, given the fact that the σ found for this carbon nanofiber PR 24 HHT XT is lower than the σ measured for PR 24 LHT XT, the PP/CNF composite shows a zT value of 6.1×10^{-8}, lower than 4.8×10^{-7} calculated for PP with 5 wt% of PR 24 LHT XT (Table S1), and 1.3×10^{-4} and 3.3×10^{-5} measured for composites of PP with 2 wt% of boron-doped SWCNTs and 2 wt% of MWCNT CNS-PEG, respectively [15,42].

3.4. Thermoelectric properties from 30 to ~100 °C

Table 4 and Fig. 6 show the σ and S from 30 to 94 °C of the samples. As outlined in the previous Section 3.3, a σ of ~37 S m^{-1} was measured for the CNF. Notably, at 94 °C, the σ increases up to ~51 S m^{-1}. Thereby, the CNFs used here show a negative temperature effect (NTC), defined as a decline in electrical resistivity when they are exposed to a rise in temperature. Therefore, the influence of temperature on the σ of these CNFs is opposite to that of other Pyrograf® III studied [18,37], which show a positive temperature effect (PTC) in the same range of temperature. On the other hand, although the PP/CNF composite also shows an NTC, its increase in σ is much more subtle in this temperature range. It is worth noting that similar behaviour has been observed in polyether ether ketone (PEEK) composites melt-mixed with 10 wt% of PR 24 LHT XT, where σ kept almost constant over the same temperature range [38]. On the contrary, a PTC effect was measured for polypropylene with 5 wt % of PR 24 LHT XT and PR 19 LHT XT [18]. From these results, it is concluded that among the different existing Pyrograf® III CNFs, the grade of CNFs used (PS, LHT and HHT) causes significant differences in the electrical behaviour of their derived PP/CNF compounds.

Fig. 6 and Table 4 presents the S from 30 to 94 °C of the samples. It is noticed that, in both cases, the S remains positive. In particular for the CNFs, it is found a S of 40.6 μVK^{-1} at 31 °C, which slightly rises to 41.8 μV K^{-1} at 94 °C, while for the PP/CNF a S of 37.6 μVK^{-1} at 30 °C, which slightly rises to 39.2 μV K^{-1} at 94 °C is observed. Interestingly, a rise of S (in absolute terms) from 40 to 100 °C was obtained for Pyrograf® III PR 25 PS XT [37], PR 24 LHT XT and PR 19 LHT XT [18]. Likewise, the increase of S obtained in the PP/CNF, was also observed in PP with 5 wt % of PR 24 LHT XT and PR 19 LHT XT [18], and PEEK with 10 wt% of PR 24 LHT XT [38]. Therefore, from all these results, it is expected an increase of S with temperature for these CNFs and their derived polymer composites in this interval of temperature.

Table 4 presents the PF of the samples analysed. The CNFs show a PF of ~6.1×10^{-2} μW m^{-1} K^{-2} (at 31 °C), which rises to ~8.8×10^{-2} μW m^{-1} K^{-2} at 94 °C. It should be noted that PR 24 LHT XT and PR 19 LHT XT show lower PF of ~4.3×10^{-3} μW m^{-1} K^{-2} at 100 °C [18], while PF of ~7.2×10^{-5} μW m^{-1} K^{-2} was calculated at 100 °C for Pyrograf® III PR 25 PS XT [37]. As previously noted, the PF of 1.0×10^{-4} μWm^{-1} K^{-2} of PP/CNF at 30 °C, increased to ~2.5×10^{-4} μW m^{-1} K^{-2} at 94 °C, below the value of 2×10^{-3} μW m^{-1} K^{-2} observed at 100 °C in PP with 5 wt% of PR 24 LHT XT [18]. Ultimately, the zT of PP/CNF composite is ~1.9×10^{-7} at 94 °C, which is below the zT of ~2.5×10^{-6} at 100 °C measured in polypropylene with 5 wt% of PR 24 LHT XT [18].

3.5. Electric modeling

As in previous works [18], to understand in more detail the electrical properties of samples, the 3D variable range hopping (VRH) model is used:

$$\boldsymbol{\sigma(T)} = \boldsymbol{e}^{\pm\left(\frac{|\boldsymbol{W_D}|}{\mathbf{k_B T}}\right)^{1/4}} \quad (2)$$

In which, the Boltzmann's constant is k_B, and W_D defines the energy potential. If $W_D > 0$, σ(T) leads to a thermally activated hopping through potential wells, causing the NTC effect, while when $W_D < 0$, σ(T) leads to a thermally activated backscattering across structural defects or impurities, causing the PTC effect [19]. In this work, the W_D of the CNFs and PP/CNF is positive with values of ~67 eV and 3×10^3 eV, respectively. In particular, the $|\boldsymbol{W_D}|$of the CNFs is ~10 times higher than the $|\boldsymbol{W_D}|$ of 0.15 eV obtained in PR 24 LHT XT [18], and ~ 10^3 times higher than $|\boldsymbol{W_D}|$ of 3.9 and 6.3 eV estimated for PP filled with 5 wt% of PR 24 LHT XT, and 5 wt% of PR 19 LHT XT, respectively [18]. It should be noticed that the Eq. (2) implies a statistical average over a distribution of energy

Table 4
TE results at all temperatures (CNFs were measured at 31 °C).

T (°C)	Sample	Conductivity (S m^{-1})	Seebeck (μV K^{-1})	Power Factor (μW m^{-1}·K^{-2})	Thermal Conductivity (W m^{-1} K^{-1})	zT
30	CNF	37 ± 2	40.6 ± 0.1	6.1×10^{-2}		4.3×10^{-5}[a]
	PP/CNF	0.07 ± 0.06	37.6 ± 0.4	1.0×10^{-4}	0.49	6.2×10^{-8}
46	CNF	39 ± 2	41.5 ± 0.3	6.7×10^{-2}		5.0×10^{-5}[a]
	PP/CNF	0.07 ± 0.05	38.4 ± 0.2	1.0×10^{-4}	0.48	6.7×10^{-8}
62	CNF	42 ± 2	41.7 ± 0.3	7.3×10^{-2}		5.7×10^{-5}[a]
	PP/CNF	0.13 ± 0.10	39.0 ± 0.4	2.0×10^{-4}	0.50	1.3×10^{-7}
78	CNF	47 ± 3	41.8 ± 0.1	8.2×10^{-2}		6.7×10^{-5}[a]
	PP/CNF	0.13 ± 0.09	39.4 ± 0.1	2.0×10^{-4}	0.49	1.4×10^{-7}
94	CNF	51 ± 2	41.8 ± 0.1	8.8×10^{-2}		7.6×10^{-5}[a]
	PP/CNF	0.16 ± 0.11	39.2 ± 0.1	2.5×10^{-4}	0.50	1.9×10^{-7}

[a] k of CNFs calculated with 0.43 W m^{-1} K^{-1} [43].

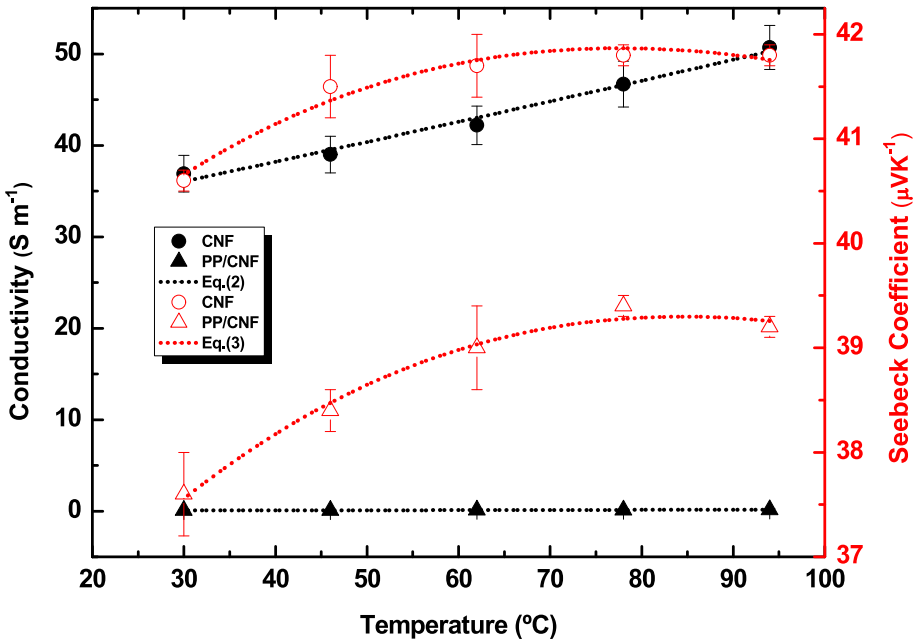


Fig. 6. σ (solid black symbols) and S (open red symbols) of CNFs and PP/CNF. The dotted curves correspond to Eq. (2) and Eq. (3).

barriers/potential wells that capture the disorder effects over electronic transport. Thus, the magnitude of W_D represents the average depth/height of the wells/barriers, while its sign correlates with the one of the charge carriers, obeying the relative position of the Fermi level to the ionization energies of the donor. Consequently, and in contrast to the previously studied Pyrograf® III CNF types, this grade of CNFs and its derived PP/CNF composite show positive W_D, which explains the positive sign of their Seebeck coefficient and the observed NTC.

Likewise, as in previous works [18], the equation utilized for studying the nonlinear behaviour of doped MWCNT mats [20] is applied here to understand deeply their S (T):

$$S(T) = bT + \frac{cT_p}{T^2}\frac{\exp\left(\frac{T_p}{T}\right)}{\left[\exp\left(\frac{T_p}{T}\right)+1\right]^2} \quad (3)$$

where, bT defines the metallic term, c is a constant, $T_p = (E_p - E_f)/k_B$, E_F is the Fermi energy level, and E_P denotes the energy of the localized states near E_F in the density of states [45]. The values of b, c, T_p and E_p - E_F using Eq. (3) are presented in Table 5. There is shown that the b of the CNFs is 6.6×10^{-3} μVK^{-2} (positive), while T_P is 824.4 K, and ($E_P - E_F$) is 7.1×10^{-2} eV. As a result, the b, T_P and ($E_P - E_F$) of the carbon nanofibers discussed here are close to the b, T_P and ($E_P - E_F$) obtained for PR 19 LHT XT and PR 24 LHT XT [18] and PR 25 PS XT [37]. On the contrary, the term c is positive for both samples, unlike the Pyrograf® III CNFs and their derived polymer composites analysed previously [18,38], which always showed negative c values. In those works, the origin of this negative sign for the c, was deduced as consequence of defects or impurities in the structure of the CNFs themselves, which cause resonances near the density of states in the E_F. It can therefore be deduced that this change of sign for c found now could be explained by the more perfect structure of this type of CNFs with fewer defects or impurities. However, it is worth noting the sign (−) of b in the composite, in contrast to positive sign (+) of b found in the carbon nanofibers. To explain this, it is noticed that the Eq. (3) defines two different behaviors. In particular, the first term/summand, bT, corresponds to nearly free charge carriers, where if b is +, then the free charge carriers are holes, while if b < 0, then they are electrons. Therefore, the b < 0 found in PP/CNF leads to suggest that PP is donating electrons (n-type doping) to CNFs, which implies a decrease in the p-type of the CNFs, and as consequence a reduction in the value of S found for the composite.

In conclusion, the σ of the composite is driven by the σ of the carbon nanofibers, and well explained in the framework of thermally activated hopping as consequence of the more perfect structure of CNFs used in this work. On the contrary, the S of the composite is not driven by the S of the carbon nanofibers, associated with possible electron transferring from PP to CNFs.

Table 5
Electric modeling, b, c, T_P and ($E_P - E_F$) estimated by Eq. (3).

Sample	b (μVK^{-2})	c (μV)	T_p (K)	E_p-E_F (eV)
CNF	6.6×10^{-3}	7.4×10^{4}	824.4	7.1×10^{-2}
PP/CNF	-6.8×10^{-3}	8.3×10^{4}	875.5	7.5×10^{-2}

4. Conclusion

PP/CNF compounds with 6 wt% of Pyrograf® III carbon nanofibers PR 24 HHT XT were morphologically, and thermally analysed using SEM, and DSC and TGA. TEM results of the CNFs confirmed that they had a tubular morphology, and their crystalline structure agrees well with hexagonal graphite. SEM images of the PP/CNF composites show that adhesion between PP and CNFs is not perfectly achieved. From DSC analysis, an increase of T_c of PP/CNF with respect to the unfilled PP is clearly observed, while TGA reveals a significant enhancement in thermal stability. In terms of their TE properties at 30 °C, the PR 24 HHT XT CNFs present a modest σ of ~37 S m^{-1}, but with a Seebeck coefficient much higher than expected for this type of CNFs, showing a value of 40.6 μVK^{-1}, thus sharing the values of some types of commercial SWCNTs. Furthermore, unlike other Pyrograf® III grades, they showed positive Seebeck as most of CNTs. A lower S of 37.6 μVK^{-1} was found for PP/CNF, assigned to the effect of the donation of electrons from polypropylene molecules to the carbon nanofibers. From 30 to 100 °C, the σ of the CNFs and the PP/CNF shows NTC character, associated to thermally activated hopping, while their S(T) increases nonlinearly with the temperature. It is concluded that, despite their similarities, the different grades of Pyrograf® III CNF available exhibit clearly different thermoelectric behaviors and have notorious influence on their derived samples.

CRediT authorship contribution statement

A.J. Paleo: Writing – original draft, Project administration, Methodology, Investigation, Funding acquisition, Formal analysis, Data curation, Conceptualization. **B. Krause:** Writing – review & editing, Validation, Supervision, Resources, Methodology, Investigation, Formal analysis, Data curation. **J.M. Mánuel:** Writing – review & editing, Resources, Methodology, Investigation, Formal analysis, Data curation. **A. M. Beltrán:** Validation, Resources, Project administration, Funding acquisition, Data curation. **A.I. Ribeiro:** Writing – review & editing, Validation, Methodology, Investigation, Formal analysis. **Maria F. Cerqueira:** Writing – review & editing, Validation, Resources, Methodology, Investigation, Formal analysis, Data curation. **E. Muñoz:** Writing – review & editing, Validation, Software, Investigation, Formal analysis. **M. Melle-Franco:** Writing – review & editing, Validation, Software, Methodology, Investigation, Formal analysis. **S. Sanchez-Valdes:** Visualization, Validation, Resources, Project administration, Methodology, Funding acquisition. **P. Pötschke:** Writing – review & editing, Supervision, Resources, Methodology, Investigation, Formal analysis.

Declaration of competing interest

The authors declare that they have no known competing financial interests or personal relationships that could have appeared to influence the work reported in this paper.

Acknowledgements

AJP would like to acknowledge national funds through FCT – Fundação para a Ciência e a Tecnologia, I.P. and Programa de Recuperação e Resiliência (PRR) through NextGeneration EU from the European Union, under the Strategic Projects UID/00264/2025 and UID/PRR/00264/2025 of the 2C2T – Centro de Ciência e Tecnologia Têxtil (doi:10.54499/UID/00264/2025 and doi:10.54499/UID/PRR/00264/2025), and support from project GreenAuto- Green Innovation for the Automotive Industry - PPS 3- Technical Textiles for the vehicle (Ref[a] C6448637037-00000013) financed by EU funds, through the Plano de Recuperação e Resiliência (PRR), managed by IAPMEI, I.P.- Agência para a Competitividade e Inovação. MMF acknowledges support within the scope of the project CICECO Aveiro Institute of Materials, UID/50011/2025 (DOI:10.54499/UID/50011/2025) & LA/P/0006/2020 (DOI:10.54499/LA/P/0006/2020), financed by national funds through the FCT/MCTES (PIDDAC). J. M.M, A. M. B. like to acknowledge the Central Services of the University of Seville, for the use of microscopy facilities.

Appendix A. Supplementary data

Supplementary data to this article can be found online at https://doi.org/10.1016/j.diamond.2026.113823.

Data availability

Data will be made available on request.

References

[1] A. Mehdizadeh Dehkordi, M. Zebarjadi, J. He, T.M. Tritt, Thermoelectric power factor: enhancement mechanisms and strategies for higher performance thermoelectric materials, Mater. Sci. Eng. 97 (2015) 1–22.
[2] X. Crispin, Thermoelectrics: carbon nanotubes get high, Nat. Energy 1 (2016) 16037.
[3] G. Tan, L.-D. Zhao, M.G. Kanatzidis, Rationally designing high-performance bulk thermoelectric materials, Chem. Rev. 116 (2016) 12123–12149.
[4] O. Bubnova, X. Crispin, Towards polymer-based organic thermoelectric generators, Energy Environ. Sci. 5 (2012) 9345–9362.
[5] X.-L. Shi, N.-H. Li, M. Li, Z.-G. Chen, Toward efficient thermoelectric materials and devices: advances, challenges, and opportunities, Chem. Rev. 125 (2025) 7525–7724.
[6] V.-H. Vo Le, C. Binet, A. Cayla, J.-F. Tahon, J.-F. Brun, V. Gaucher, In-plane vs through-plane electrical conductivity of poly(lactic acid)/multiwalled carbon nanotubes: impact on thermoelectric properties, ACS Appl. Polym. Mater. 6 (2024) 14365–14376.
[7] L. Yu, X. Liu, B. Zhang, H. Hu, K. Chen, H. Li, D.J.S. Birch, Y. Chen, H. Qiu, P. Gu, Phase-transition-promoted thermoelectric textiles based on twin surface-modified CNT fibers, ACS Appl. Mater. Interfaces 16 (2024) 18030–18039.
[8] S. Han, S. Chen, F. Jiao, Insulating polymers for flexible thermoelectric composites: a multi-perspective review, Compos. Commun. 28 (2021) 100914.
[9] Z. Wang, W. Jiang, P. Cao, Y. Wang, A.-Q. Xie, S. Niu, Y. Xu, L. Li, K.-Q. Zhang, X.-Q. Wang, Bioinspired programmable and ultrastretchable janus helical hydrogel fibers for strain-invariant thermoelectric body heat harvesting and sensation, Nano Lett. 25 (2025) 2509–2518.
[10] S.K.H. Gulrez, M.E. Ali Mohsin, H. Shaikh, A. Anis, A.M. Pulose, M.K. Yadav, E.H. P. Qua, S.M. Al-Zahrani, A review on electrically conductive polypropylene and polyethylene, Polym. Compos. 35 (2014) 900–914.
[11] N.T. Hung, A.R.T. Nugraha, R. Saito, Thermoelectric properties of carbon nanotubes, Energies 12 (2019) 4561.
[12] S. Zhou, X.-L. Shi, L. Li, Q. Liu, B. Hu, W. Chen, C. Zhang, Q. Liu, Z.-G. Chen, Advances and outlooks for carbon nanotube-based thermoelectric materials and devices, Adv. Mater. 37 (2025) 2500947.
[13] B. Krause, C. Barbier, K. Kunz, P. Pötschke, Comparative study of singlewalled, multiwalled, and branched carbon nanotubes melt mixed in different thermoplastic matrices, Polymer 159 (2018) 75–85.
[14] T. Khan, M.S. Irfan, M. Ali, Y. Dong, S. Ramakrishna, R. Umer, Insights to low electrical percolation thresholds of carbon-based polypropylene nanocomposites, Carbon 176 (2021) 602–631.
[15] B. Krause, C. Barbier, J. Levente, M. Klaus, P. Pötschke, Screening of different carbon nanotubes in melt-mixed polymer composites with different polymer matrices for their thermoelectrical properties, J. Compos. Sci. 3 (2019) 106.
[16] A.J. Paleo, B. Krause, M.F. Cerqueira, M. Melle-Franco, P. Pötschke, A.M. Rocha, Thermoelectric properties of polypropylene carbon nanofiber melt-mixed composites: exploring the role of polymer on their Seebeck coefficient, Polym. J. 53 (2021) 1145–1152.
[17] J.-P. Tessonnier, D. Rosenthal, T.W. Hansen, C. Hess, M.E. Schuster, R. Blume, F. Girgsdies, N. Pfänder, O. Timpe, D.S. Su, R. Schlögl, Analysis of the structure and chemical properties of some commercial carbon nanostructures, Carbon 47 (2009) 1779–1798.
[18] A.J. Paleo, B. Krause, A.R. Mendes, C.J. Tavares, M.F. Cerqueira, E. Muñoz, P. Pötschke, Comparative thermoelectric properties of polypropylene composites melt-processed using Pyrograf® III carbon nanofibers, J. Compos. Sci. 7 (2023) 173.
[19] N.F. Mott, Conduction in glasses containing transition metal ions, J. Non-Cryst. Solids 1 (1968) 1–17.
[20] Y.M. Choi, D.S. Lee, R. Czerw, P.W. Chiu, N. Grobert, M. Terrones, M. Reyes-Reyes, H. Terrones, J.C. Charlier, P.M. Ajayan, S. Roth, D.L. Carroll, Y.W. Park, Nonlinear behavior in the thermopower of doped carbon nanotubes due to strong, localized states, Nano Lett. 3 (2003) 839–842.
[21] T.N. Tallman, The effect of thermal loading on negative permittivity in carbon nanofiber/silicone metacomposites, Mater. Today Commun. 22 (2020) 100843.
[22] J.M. Muñoz-Ávila, S. Sánchez-Valdes, I. Yáñez-Flores, O.S. Rodriguez-Fernandez, M.G. Neira-Velázquez, E. Hernández-Hernández, S. Flores-Gallardo, F. Avalos-Belmontes, T. Lozano-Ramírez, A. Morales-Cepeda, P.G. Lafleur, Influence of carbon nanofiber functionalization and compatibilizer on the physical properties of carbon nanofiber reinforced polypropylene nanocomposites, Polym. Compos. 39 (2018) 3575–3585.
[23] W. Jenschke, M. Ullrich, B. Krause, P. Pötschke, Messanlage zur Untersuchung des Seebeck-Effektes in Polymermaterialien vol. 87, Technisches Messen, 2020, pp. 495–503.
[24] B. Krause, P. Pötschke, Polyethylene glycol as additive to achieve n-conductive melt-mixed polymer/carbon nanotube composites for thermoelectric application, Nanomaterials 12 (2022) 3812.
[25] A.J. Paleo, V.M. Serrato, J.M. Mánuel, O. Toledano, E. Muñoz, M. Melle-Franco, B. Krause, P. Pötschke, K. Lozano, Doping effect of poly(vinylidene fluoride) on carbon nanofibers deduced by thermoelectric analysis of their melt mixed films, Chin. J. Polym. Sci. 42 (2024) 1802–1810.
[26] S. Spicher, S. Grimme, Robust atomistic modeling of materials, organometallic, and biochemical systems, Angew. Chem. Int. Ed. 59 (2020) 15665–15673.
[27] S. Grimme, C. Bannwarth, P. Shushkov, A robust and accurate tight-binding quantum chemical method for structures, vibrational frequencies, and noncovalent interactions of large molecular systems parametrized for all spd-block elements (Z = 1–86), J. Chem. Theory Comput. 13 (2017) 1989–2009.
[28] A.V. Marenich, S.V. Jerome, C.J. Cramer, D.G. Truhlar, Charge model 5: an extension of hirshfeld population analysis for the accurate description of molecular interactions in gaseous and condensed phases, J. Chem. Theory Comput. 8 (2012) 527–541.
[29] C. Bannwarth, E. Caldeweyher, S. Ehlert, A. Hansen, P. Pracht, J. Seibert, S. Spicher, S. Grimme, Extended tight-binding quantum chemistry methods, WIREs Comput. Mol. Sci. 11 (2021) e1493.
[30] P. Trucano, R. Chen, Structure of graphite by neutron diffraction, Nature 258 (1975) 136–137.
[31] S. Bernal, F.J. Botana, J.J. Calvino, C. López-Cartes, J.A. Pérez-Omil, J. M. Rodríguez-Izquierdo, The interpretation of HREM images of supported metal

catalysts using image simulation: profile view images, Ultramicroscopy 72 (1998) 135–164.
[32] K. Harada, P. Chu, K. Xu, A. Fujimori, Polypropylene-based nanocomposite with improved mechanical properties: effect of cellulose nanofiber and polyrotaxane with partial miscibility, Polym. Compos. 44 (2023) 2977–2987.
[33] A. de la Vega Oyervides, J.B. Ríos, L.F.R. de Valle, L.A.S.d.A. Prado, K. Schulte, Peroxide assisted coupling and characterization of carbon-nanofiber-reinforced Poly(propylene) composites, Macromol. Mater. Eng. 292 (2007) 1095–1102.
[34] R. Cruz-Silva, J. Romero-García, J.L. Angulo-Sánchez, Nucleation activity of polyaniline coated short glass fiber towards isotactic polypropylene, J. Mater. Sci. 40 (2005) 5107–5109.
[35] M.-K. Seo, J.-R. Lee, S.-J. Park, Crystallization kinetics and interfacial behaviors of polypropylene composites reinforced with multi-walled carbon nanotubes, Mater. Sci. Eng. A 404 (2005) 79–84.
[36] A.J. Paleo, B. Krause, M.F. Cerqueira, E. Muñoz, P. Pötschke, A.M. Rocha, Nonlinear thermopower behaviour of N-type carbon nanofibres and their melt mixed polypropylene composites, Polymers 14 (2022) 269.
[37] A.J. Paleo, B. Krause, M.F. Cerqueira, J.M. González-Domínguez, E. Muñoz, P. Pötschke, A.M. Rocha, Thermoelectric properties of cotton fabrics dip-coated in pyrolytically stripped Pyrograf® III carbon nanofiber based aqueous inks, Materials 16 (2023) 4335.
[38] A.J. Paleo, B. Krause, D. Soares, M. Melle-Franco, E. Muñoz, P. Pötschke, A. M. Rocha, Thermoelectric properties of N-type poly (ether ether ketone)/carbon nanofiber melt-processed composites, Polymers 14 (2022) 4803.
[39] S. Lee, J.R. Hahn, B.-C. Ku, J. Kim, Effect of carbon nanofiber structure on crystallization kinetics of polypropylene/carbon nanofiber composites 32 (7) (2011) 2369–2376.
[40] G.M. Koo, T.N. Tallman, Frequency-dependent alternating current piezoresistive switching behavior in self-sensing carbon nanofiber composites, Carbon 173 (2021) 384–394.
[41] K. Bradley, S.-H. Jhi, P.G. Collins, J. Hone, M.L. Cohen, S.G. Louie, A. Zettl, Is the Intrinsic thermoelectric power of carbon nanotubes positive? Phys. Rev. Lett. 85 (2000) 4361–4364.
[42] B. Krause, V. Bezugly, V. Khavrus, L. Ye, G. Cuniberti, P. Pötschke, Boron doping of SWCNTs as a way to enhance the thermoelectric properties of melt-mixed polypropylene/SWCNT composites, Energies 13 (2020) 394.
[43] N.K. Mahanta, A.R. Abramson, M.L. Lake, D.J. Burton, J.C. Chang, H.K. Mayer, J. L. Ravine, Thermal conductivity of carbon nanofiber mats, Carbon 48 (2010) 4457–4465.
[44] C.A. Hewitt, A.B. Kaiser, S. Roth, M. Craps, R. Czerw, D.L. Carroll, Varying the concentration of single walled carbon nanotubes in thin film polymer composites, and its effect on thermoelectric power, Appl. Phys. Lett. 98 (2011).
[45] G.D. Mahan, Impurity resonances in carbon nanotubes, Phys. Rev. B 69 (2004) 125407.